

Characterization of single thyroid nodules by contrast-enhanced 3-D ultrasound

*Original*

Characterization of single thyroid nodules by contrast-enhanced 3-D ultrasound / Molinari, Filippo; Mantovani, A.; Deandrea, M.; Limone, P.; Garberoglio, R.; Suri, J. S.. - In: ULTRASOUND IN MEDICINE AND BIOLOGY. - ISSN 0301-5629. - STAMPA. - 36:10(2010), pp. 1616-1625. [10.1016/j.ultrasmedbio.2010.07.011]

*Availability:*

This version is available at: 11583/2373466 since:

*Publisher:*

Elsevier

*Published*

DOI:10.1016/j.ultrasmedbio.2010.07.011

*Terms of use:*

This article is made available under terms and conditions as specified in the corresponding bibliographic description in the repository

*Publisher copyright*

(Article begins on next page)

# CHARACTERIZATION OF SINGLE THYROID NODULES BY CONTRAST-ENHANCED 3-D ULTRASOUND

FILIPPO MOLINARI,<sup>\*</sup> ALICE MANTOVANI,<sup>\*</sup> MAURILIO DEANDREA,<sup>†</sup> PAOLO LIMONE,<sup>†</sup>  
ROBERTO GARBEROGLIO,<sup>‡</sup> and JASJIT S. SURI<sup>§||</sup>

<sup>\*</sup>Biolab, Department of Electronics, Politecnico di Torino, Torino, Italy; <sup>†</sup>Endocrinology Section, “Umberto I” Hospital, Ordine Mauriziano di Torino, Torino, Italy; <sup>‡</sup>Fondazione Scientifica Mauriziana ONLUS, Torino, Italy; <sup>§</sup>Biomedical Technologies Inc., Denver, CO, USA; and <sup>||</sup>Idaho State University, Pocatello, ID, USA

**Abstract**—High-resolution ultrasonography (HRUS) has potentialities in differential diagnosis between malignant and benign thyroid lesions, but interpretative pitfalls remain and accuracy is still poor. We developed an image processing technique for characterizing the intra-nodular vascularization of thyroid lesions. Twenty nodules (10 malignant) were analyzed by three-dimensional (3-D) contrast-enhanced ultrasound imaging. The 3-D volumes were preprocessed and skeletonized. Seven vascular parameters were computed on the skeletons: number of vascular trees (NT); vascular density (VD); number of branching nodes (or branching points) (NB); mean vessel radius (MR); 2-D (DM) and 3-D (SOAM) tortuosity; and inflection count metric (ICM). Results showed that the malignant nodules had higher values of NT (83.1 vs. 18.1), VD (0.4 vs. 0.01), NB (1453 vs. 552), DM (51 vs. 18), ICM (19.9 vs. 8.7) and SOAM (26 vs. 11). Quantification of nodular vascularization based on 3-D contrast-enhanced ultrasound and skeletonization could help differential diagnosis of thyroid lesions. (E-mail: [filippo.molinari@polito.it](mailto:filippo.molinari@polito.it))

**Key Words:** Contrast-enhanced ultrasound, Thyroid nodule, Skeleton, Vascular assessment, Tumor.

## INTRODUCTION

Thyroid nodules are common findings in clinical practice and occur in more than 50% of adult population; nevertheless, only 7% of thyroid nodules are malignant ([Hoang et al. 2007](#)). High-resolution ultrasonography (HRUS) is the most frequently used tool for identification, assessment and follow-up of thyroid lesions ([Fig. 1a](#)). This is because it can reveal formations as small as 1 mm, is noninvasive and is not expensive ([Polyzos et al. 2007](#)). Even though it has been demonstrated that malignancy is related to common features in HRUS B-Mode images (*i.e.*, microcalcifications, marked hypoechogenicity, irregular margins and the absence of a hypoechoic halo around the nodule [[Bastin et al. 2009](#)]), interpretative pitfalls remain. Recently, [D’Souza et al.](#) measured the HRUS sensitivity and specificity in 80.8% and 81.6%, respectively ([D’Souza et al. 2010](#)), thus, demonstrating limited performance in detecting malignancy.

Color Doppler ultrasound imaging ([Fig. 1b](#)) has been used to differentiate thyroid nodules. Results showed that benign nodules tend to have no or minimal internal flow with presence or absence of a peripheral ring, whereas malignant nodules tend to have a peripheral ring with an extensive internal flow ([Ivanac et al. 2007](#)). These studies evidenced the need for a quantitative evaluation of the internal nodule flow, to avoid subjective interpretations and partial visions.

Contrast-enhanced ultrasound imaging (CEUS) has been introduced to improve the differential diagnosis of thyroid nodules. The contrast agent enhances the parenchyma representation, given the abundant vasculature of the thyroid gland. Therefore, by using CEUS, it is possible to gain a better representation of the thyroid vascular pattern, overcoming the limitations given by the low spatial resolution of color Doppler imaging ([Fig. 1c](#)). CEUS studies of the thyroid nodules, conducted by analyzing the increase in the echogenicity of the nodule due to perfusion, did not prove more performing than traditional HRUS ([Bartolotta et al. 2006](#)). On the contrary, CEUS perfusion analysis of neoplastic nodules proved effective in differentiating benign from malignant

---

Address correspondence to: Filippo Molinari, Ph.D., Biolab – Dipartimento di Elettronica, Politecnico di Torino, Corso Duca degli Abruzzi, 24, 10129 Torino, Italy. E-mail: [filippo.molinari@polito.it](mailto:filippo.molinari@polito.it)

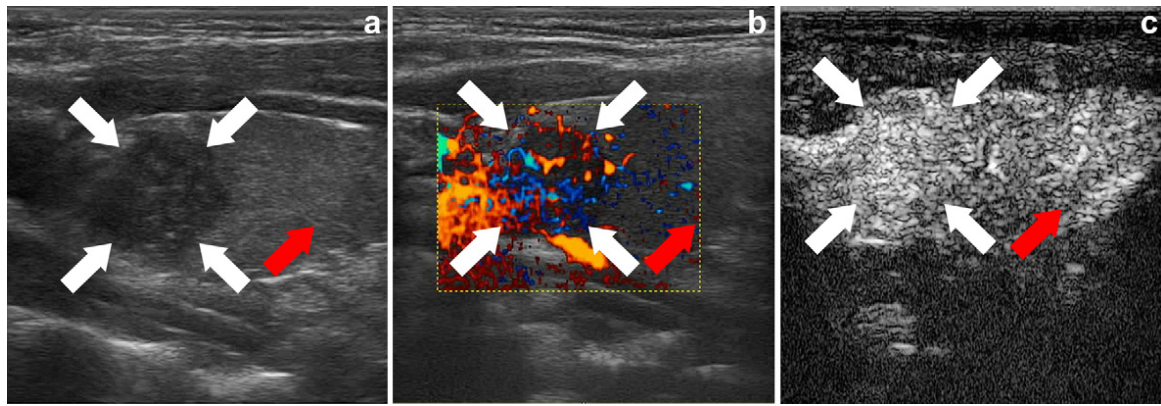


Fig. 1. (a) High-resolution ultrasonography (HRUS) image of a papillary carcinoma. The white arrow indicates the nodule; the red arrow indicates the healthy thyroid parenchyma. (b) Color Doppler image of the papillary carcinoma showing marked vascularization of the lesion (white arrows) compared with healthy parenchyma (red arrow). (c) Contrast-enhanced ultrasound imaging (CEUS) image of the papillary carcinoma showing marked enhancement of the lesion (white arrows) compared with healthy parenchyma (red arrow). All three images are same projection and slice.

lesions, even if performances were poor compared with fine needle aspiration examinations (Appetecchia et al. 2006). CEUS enhancement patterns were found different in benign and malignant lesions, and ring enhancement was indicative of benign lesions, whereas heterogeneous enhancement was indicative of malignancy (Zhang et al. 2010).

The purpose of our study was to develop a methodology for the 3-D analysis of thyroid nodules and for an objective representation and numerical characterization of the 3-D nodular vascularization. Earlier studies we conducted (Carraro et al. 2008; Molinari et al. 2008) showed that color and power Doppler imaging were not suitable for 3-D micro-vessel detection, due to poor spatial resolution and to color blooming that may occur in highly perfused nodules (blooming can be seen in Fig. 1b). We used CEUS and developed a processing technique to represent the 3-D internal flow that we used to characterize 20 solitary thyroid nodules. This methodology represents a step forward with respect to an earlier study we started in 2008 (Carraro et al. 2008). In our former procedure, the characteristics of the 3-D CEUS images were qualitatively scored by an expert sonographer whereas in this study, we will show our numerical approach to describe the internal nodular vasculature.

## MATERIALS AND METHODS

### *Image acquisition and patients*

We enrolled in this study 30 patients with a previous diagnosis of thyroid nodule. We excluded patients having multi-nodule goiter. We preselected subjects showing HRUS features of malignancy: intra-nodular micro-calcifications, hypoechoic appearance and irregular

margins (Bastin et al. 2009). Patients were thus nonconsecutive. All the patients signed an informed consent prior of participating in the experiment. The experimental protocol was approved by the ethical committee of the Endocrinology Section of the “Umberto I” Hospital of Torino (Italy).

All the subjects underwent a clinical examination, hormonal profile and ultrasound (HRUS and color Doppler) examination of the lesion. Then, a bolus of 2.5 mL of ultrasound contrast agent (Sonovue; Bracco Imaging, Milano, Italy) was administered intravenously and a gray-scale 3-D volume containing the lesion was acquired. Due to bulkiness and weight of external mechanical scanning systems and the variability associated with the nodules dimension and its position, we preferred to perform freehand scanning. A trained operator with more than 30 years of experience in neck ultrasonography (R.G.) performed all the scans 50 s after the injection of the contrast agent bolus. The freehand scanning was performed by sliding the probe along the patient’s neck to cover the nodule extension. The high frame rate of the device compared with the slow movement of the probe ensured that there was no gap between adjacent frames. The average frame rate of the device during acquisitions was 16 frames/s.

Images were acquired by a MyLab70 ultrasound scanner (Biosound-Esaote, Genova, Italy) equipped by a LA-522 linear probe working in the range 4–10 MHz. All the images were acquired at 5 MHz. We calibrated gain by acquiring an empty volume (probe in air) and set the background average intensity to be less than 5 in a linear scale 0–255. Gain was constant for all patients. The TGC curve was set to flat in the middle of the scale and kept constant. The volumes were transferred in DICOM format to an external workstation Apple

PowerPc (Apple, Cupertino, CA, USA), dual 2.5 GHz, 8 GB of RAM and equipped with processing and reconstruction software.

All the subjects underwent ultrasound-guided fine needle aspiration biopsy (FNAB) of the thyroid lesion. Five nodules were benign (goiter nodules) and classified as THY2 according to cytologic criteria (Mihai et al. 2009). In 25 nodules, cytology suggested a follicular neoplasm (THY3). These patients underwent thyroidectomy. We eliminated from the study five patients who had a nodule of diameter greater than 6 cm, which was twice the average size of the other nodules and, which caused problems in manual scanning. Three patients were eliminated due to motion artifacts during the CEUS examination (swallowing and cough). Two patients were eliminated since FNAB demonstrated a concomitant thyroiditis. Of the 15 THY3 patients, five had benign (follicular neoplasm) and ten malignant (seven papillary, one follicular and two Hurtle cells carcinoma) results. Overall, we had ten benign and ten malignant lesions.

The results of the FNAB (or of the histopathologic analysis for surgically removed tumors) were kept blinded to the researchers until the image acquisitions and processing were completed.

Ten subjects were males (age:  $53.5 \pm 13.3$  years; range: 22–71 years) and 10 females (age:  $50.1 \pm 10.8$  years; range: 25–68 years). The average size of the nodules was  $31.7 \pm 17.9$  mm, range: 10–52 mm (malignant:  $34.4 \pm 18.8$  mm; benign:  $29.3 \pm 17.3$  mm).

#### CEUS image processing strategy

The image processing system (ThyScreenCEUS) we developed was structured in three main steps: (1) image preprocessing; (2) morphologic aperture for contrast agent bubbles detection; and (3) thresholding and 3-D lesion reconstruction. Figure 2 depicts the steps of the algorithm on a malignant thyroid nodule (papillary carcinoma).

#### Preprocessing

All the images of the 3-D volume were first converted into double precision format. When we insonated a homogeneous phantom with the same probe and the same settings that were used in the study, we found a linear dependence of the average gray level from depth (*i.e.*, from the vertical dimension of the image). A linear ramp with decreasing intensity from 1 to 0 was applied to the original image (Fig. 2a) to attenuate the intensity artifact that was present in the distal (*i.e.*, deeper) portion of the images (the result after intensity correction in Fig. 2b).

To make the algorithm as independent as possible on the acquisition scanner/probe and on the optical

integrated density of the image (due to different concentrations of the contrast agent in the 3-D slices), each image was normalized. Non-perfused zones were mapped to black; highly perfused regions were mapped to white. This step required the manual selection of two  $3 \times 3$  ROIs on an image of the 3-D volume.

The images were then low-pass filtered by using a  $7 \times 7$  Gaussian kernel with standard deviation of 0.1 pixels. Finally, speckle noise was attenuated by using the first order local statistic filter, defined by the following equation:

$$J_{x,y} = \bar{I} + k_{x,y}(I_{x,y} - \bar{I})$$

where,  $I_{x,y}$  is the intensity of the noisy pixel,  $\bar{I}$  is the mean intensity of a  $N \times M$  pixel neighborhood and  $k_{x,y}$  is a local statistic measure. The noise-free pixel is indicated by  $J_{x,y}$ . We followed the proposal by Loizou et al. (Loizou et al. 2005), who defined  $k_{x,y} = \frac{\sigma_I^2}{\bar{I}^2 \sigma_I^2 + \sigma_n^2}$ , where  $\sigma_I^2$  represents the variance of the pixels in the neighborhood and  $\sigma_n^2$  the variance of the noise in the cropped image. We found that a suitable neighborhood size was  $7 \times 7$ . The normalized, filtered and despeckled image is reported in Figure 2c.

#### Microbubble detection using morphologic aperture

To detect the microbubbles in the acquired volume, we processed every 2-D slice separately. The images had an axial resolution of  $62.5 \mu\text{m}/\text{pixel}$  and the contrast agent was constituted by microbubbles of less than  $10 \mu\text{m}$  diameter (Gorce et al. 2000). Hence, we used a structuring element consisting of a disk with radius of 5 pixels, which gave maximum sensibility on groups of microbubbles. The images were then morphologically opened (Fig. 2d).

#### Threshold process and 3-D reconstruction

Threshold process was used to create a mask for each volumetric slice. At this stage, we considered the image histogram composed of two Gaussians, one relative to the foreground (*i.e.*, the presence of microbubbles) and the other relative to the background (*i.e.*, the absence of microbubbles). Thus, this is a two-class problem. Since a threshold can separate the statistical distribution of the two classes, Otsu's method was adopted. The threshold was made local since it was computed separately for each frame of the 3-D volume. Figure 2e and Fig. 2f depict the obtained segmentation mask and the final segmentation, respectively.

The original 3-D volume was then multiplied by the segmentation masks and was reconstructed to spatially visualize the distribution of contrast agent in the thyroid lesion (we used OsiriX software – <http://www.osirix-viewer.com/> by the Osirix Foundation, Genève, Switzerland).



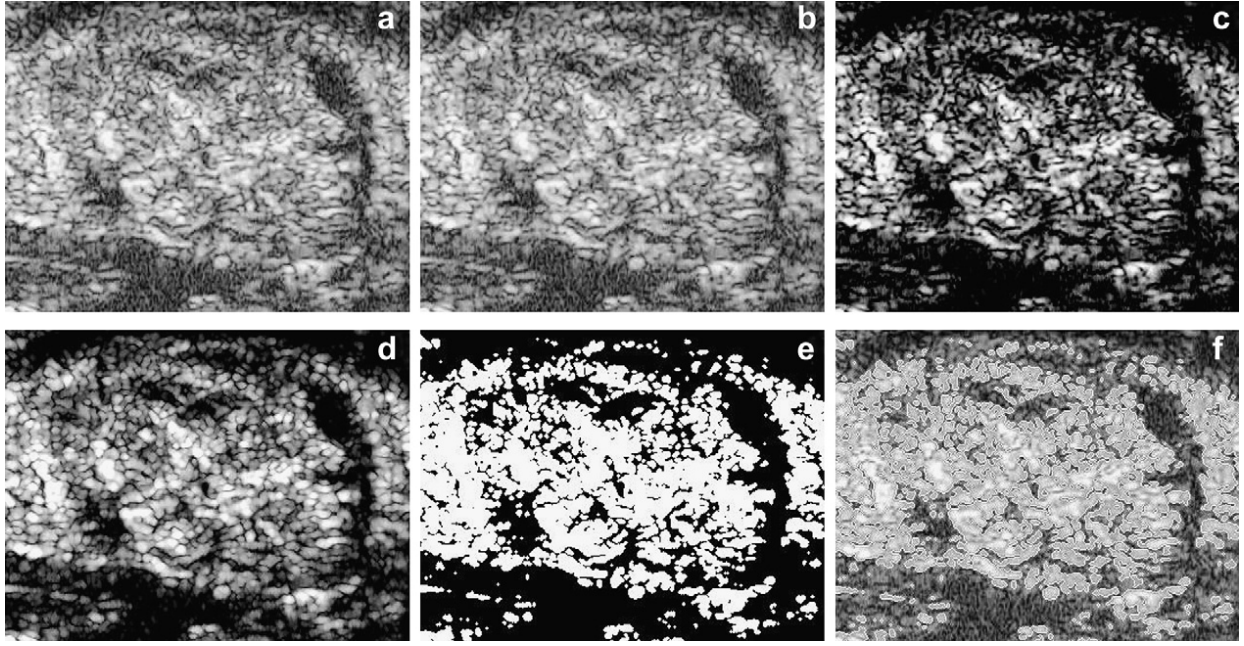


Fig. 2. Processing of a single frame of the 3-D volume of a thyroid nodule. (a) Raw image. (b) Image after the application of a linear ramp to compensate the depth artifact. (c) Intensity normalized image. (d) Morphologic opening with a disk-shaped structuring element of 5 pixel radius. (e) Segmentation mask obtained by thresholding. (f) Contour of the segmentation overlapped to the original image.

#### *Skeletonization strategy*

The skeletonization procedure aims at reducing the amount of information in an image into a simpler image that still preserve morphology. In other words, the skeletonization is a technique for extracting the innermost and essential information of an image (Ma and Sonka 1996).

We applied skeletonization technique to our images to reduce the representation of the contrast agent in the nodule. Specifically, since the spatial resolution of our probe was more than 10 times lower than the microbubble diameter, we could only track microbubbles that were grouped together. Hence, the contrast agent diffusion in the thyroid was still over-represented and little useful from a clinical point of view. We adopted a skeletonization procedure that ensured an effective reduction of the vessels appearance while preserving connectivity.

We adopted the skeletonization technique proposed by Ma and Sonka in 1996 (Ma and Sonka 1996). This algorithm was a 3-D technique for thinning and reconstruction of binary images that was applied to medical images. This algorithm defined four classes (called A, B, C and D in the original algorithm) that were used to derive templates. Each class was translated so that a total number of 38 templates could be derived (6 templates from class A, 12 from B, 8 from C and 12 from D). A template was a cube of  $3 \times 3 \times 3$  pixels. In each voxel of the template, there was a coded number that specified the presence of the background (mapped by the 0), of the foreground

(mapped by 1), or a “don’t care” voxel (mapped by -1). Therefore, the 38 templates test each point of the image (or volume) and the point was deleted if it matched one of the templates. Full details about the Ma and Sonka algorithm (Ma and Sonka 1996) can also be found in the study by Palágyi et al. (Palágyi and Kuba 1998).

Previous studies showed that this skeleton technique does not preserve connectivity (Wang and Basu 2007). In our study, however, connectivity was the key to correctly reconstruct the vascularization of a lesion. Therefore, we modified the Ma and Sonka algorithm by inserting a preliminary skeletonization based on distance transform (DT).

The DT of a point belonging to an object is defined as its lower distance from the borders of the object. Therefore, points located in the middle of a vessel have high values of DT, whereas points located near the vessel borders have low DT values. Let  $DTI$  be an image containing the DT of each point. A point is assigned to the skeleton if its distance from the borders differs from the average distance of its neighborhood less than a predefined threshold  $T_p$ . We can express the definition of such skeleton by using the following formula:

$$DSk = DTI_F < (DTI - T_p) \quad (1)$$

where  $DSk$  is the skeleton image and  $DTI_F$  is the  $DTI$  image after a low-pass filtering with a 3-D  $10 \times 10 \times 10$  Gaussian kernel (with sigma value equal to 1).

To select the optimal value of  $T_p$ , we randomly selected four nodules (two carcinomas and two goiter nodules) from the image database. The images were skeletonized using  $T_p$  values equal to 0.40, 0.45, 0.50, 0.55, 0.60, 0.65 and 0.70. After having obtained the skeleton, we counted the total number of white points (*i.e.*, the total number of pixels constituting the skeleton). We averaged the computed number of white points on the four nodules (Fig. 3a). The curve showed an inflection for middle values of  $T_p$ . We also computed the fifth order polynomial curve fitting the white points  $T_p$  curve (Fig. 3b). The gradient showed a marked increase for a  $T_p$  value of 0.55. Therefore, we selected 0.55 as optimal value for our skeletonization procedure.

Qualitative results repeated on all the remaining images confirmed that skeletons with higher  $T_p$  values were poor of information (*i.e.* very thinned) and computationally heavy. Conversely, skeletons obtained with lower  $T_p$  values resulted in too noisy representations, even if computation time was reduced.

The summary of skeletonization procedure consisted of the following steps:

- (1) DT was applied to the 3-D CEUS image. This step roughly removed the smallest objects and cleaned the points located far from the middle of the vessels.
- (2) Application of the Ma and Sonka (Ma and Sonka 1996) skeleton. This technique considered five consecutive frames to preserve connectedness (*i.e.*, for each frame, the two preceding and the two successive frame, thus, a total of five). The points that matched one or more of the 38 templates were removed and the skeletonized frame was saved.
- (3) The step 2 was repeated for each frame until there were no more points to remove.

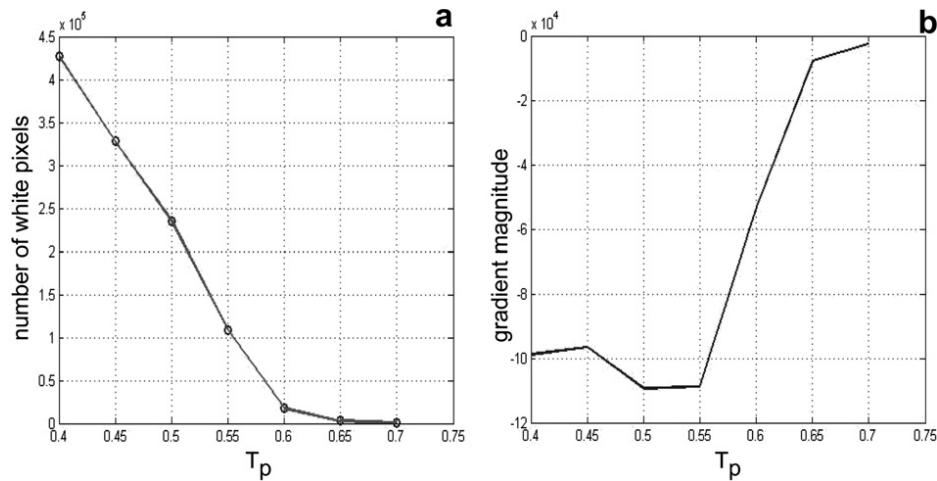


Fig. 3. (a) The graph shows the average number of points belonging to the skeleton of four randomly selected nodules (two malignant and two benign) with respect to the selectivity threshold  $T_p$ . The curve shows an inflection for middle values of  $T_p$ . (b) The gradient of the image shows a marked increase after 0.55. The  $T_p$  values considered as optimal was chosen equal to 0.55.

The DT thinning procedure, which is faster even if less accurate, allowed for a quick removal of small objects and points far from the vessel centerline, whereas the Ma and Sonka skeleton enabled an accurate reduction of the points. The use of DT prior to the application of the Ma and Sonka skeleton also reduced the computational cost of the algorithm. Figure 4 reports a sample result of the skeleton technique, showing a nodular vascularization greater than that of normal tissue.

#### Skeleton characteristics

The skeleton characteristics were analyzed and computed to provide a quantitative measure of the thyroid vascularization. In fact, considering the skeleton as the minimal representation of the thyroid lesion vascularization, we depicted that the skeleton characteristics modeled the lesion morphology.

The skeleton is a binary 3-D image containing “1” in correspondence of the contrast agent (*i.e.*, therefore of a vessel) and “0” otherwise. Hence, the skeleton can be thought of as a set of paths, some of which are connected. Many techniques were proposed to analyze the skeleton characteristics (Chen and Molloy 2002; Huang 2008). We used the breadth first search (BFS) technique. The BFS technique consists in searching all the skeleton nodes starting from a given node. The procedure iterates on all the nodes and stops when all the nodes have been visited. The BFS algorithm maps the skeleton as a series of vascular trees ( $T$ ):

$$DSk = \{T_1, T_2, \dots, T_N\} \quad (2)$$

where  $N$  is the number of the vascular trees. Each vascular tree  $T_i$  can be thought as the sequence of  $m$  nodes  $p_j$ :  $T_i = \{p_1, p_2, \dots, p_m\}$ .

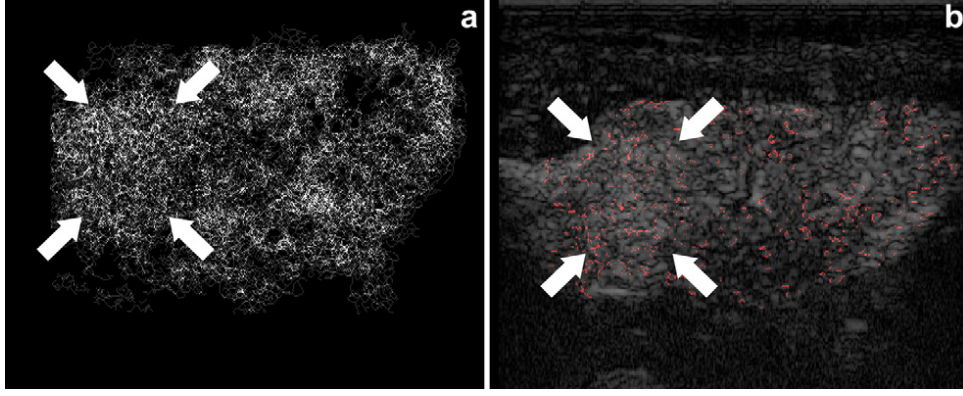


Fig. 4. (a) Maximum intensity projection (MIP) of the 3-D skeleton. (b) Contrast-enhanced ultrasound imaging (CEUS) image of a papillary carcinoma (background) with corresponding skeleton overlaid in red (for a single slice). The white arrows indicate the nodule position. The lesion shows increased vascularity with respect to healthy thyroid tissue.

By using the BFS, we computed the following skeleton characteristics (Huang et al. 2008):

- (1) Number of vascular trees (NT): defined as the number of trees in which the BFS decomposes the skeleton image. This parameter is important since we expect a higher number of vascular trees in malignant lesions compared with benign lesions.
- (2) Density of the vascular structure (VD): defined as the number of white points belonging to the skeleton ( $M$ ) over the size of the ROI. Considering a ROI of dimensions  $h, l$  and  $w$ , we can, thus, define  $VR = M / (h \cdot l \cdot w)$ . This parameter is expected to be higher in malignant lesions than in benign.
- (3) Number of branching nodes (NB): defined as the number of branches of the structure. Again, given the characteristics of the malignant neovascularization, we expect that NB is higher for tumors than for nonmalignant nodules.
- (4) Average vessel radius (MR): defined as the average radius of the vessels in the ROI. Once a set of connected vessels has been defined, the average vessel radius is calculated for each vessel by summing the radius defined at each vessel skeleton point and by dividing by the number of points. The vessels created by a tumor should have lower MR than normal vessels.
- (5) 2-D vascular tortuosity (distance metrics – DM): this is a measure of the tortuosity of a vascular tree  $T_i$ . DM can be defined as the Euclidean distance between the first and the last point of a tree divided by its real length. Let us consider a tree consisting of  $m$  nodes:  $T_i = \{p_1, p_2, \dots, p_m\}$ . The DM can be defined as:  $DM = \frac{|p_m - p_1|}{\sum_{i=1}^{m-1} |p_i - p_{i+1}|}$ , where  $|\cdot|$  denotes the Euclidean distance measure.
- (6) Inflection count metric (ICM): defined as DM divided by the number of flexes in the path. This parameter is an estimate of the average number of times the

vascular tree changes its shape from convex to concave and vice-versa.

- (7) 3-D vascular tortuosity (sum of angles metric – SOAM): this parameter is used to evaluate the vessel torsion in 3-D. With reference to Figure 5, consider a node  $p_k$ , and the two adjacent nodes  $p_{k-1}$  and  $p_{k+1}$ . Let  $V_1$  and  $V_2$  be the vectors connecting the three nodes as in Figure 5. The planar angle  $IP_k$  between the vectors  $V_1$  and  $V_2$  can be expressed as  $IP_k = \cos^{-1} \left( \left( \frac{V_1}{|V_1|} \right) \cdot \left( \frac{V_2}{|V_2|} \right) \right)$ . The angle defining the torsion of the curve in a node  $p_k$  can be expressed as  $TP_k = \cos^{-1} \left( \left( \frac{V_1 \times V_2}{|V_1 \times V_2|} \right) \cdot \left( \frac{V_2 \times V_3}{|V_2 \times V_3|} \right) \right)$ , where  $V_3$  is the vector between the nodes  $p_{k+1}$  and  $p_{k+2}$ . The total angle in a node  $p_k$  is then defined as  $CP_k = \sqrt{IP_k^2 + TP_k^2}$ . Hence, the SOAM can be computed by averaging the total angle on all the nodes of the path  $SOAM = \frac{\sum_{k=1}^{m-1} CP_k}{\sum_{k=1}^{m-1} |p_k - p_{k+1}|}$ , where  $m$  is the number of nodes of the considered path.

The skeletonization procedure was applied to the entire thyroid volume. We manually selected a cubic

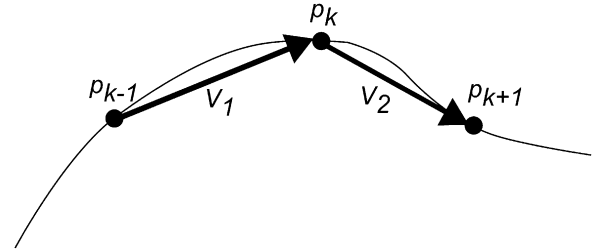


Fig. 5. Schematic representation of the SOAM computation. The vectors  $V_1$  and  $V_2$  define the planar angle  $IP_k$ , relative to the node  $p_k$ . By extending such computation to the 3-D geometry and then to all the  $m$  nodes of the path, it is possible to compute the SOAM.



ROI of  $90 \times 90 \times 20$  pixels in size centered on the lesion and we computed the seven skeleton characteristics only in the traced ROI. The dimension of the ROI was chosen by considering the average size of a thyroid lesion, which resulted in about  $150 \times 150$  pixels and in a number of slices ranging between 20 and 35. Our ROI was smaller than the average nodule size, so that it comprised a significant portion of the lesion without incorporating parenchyma pixels. This ROI size was compatible with all the lesions in our database.

## RESULTS

The average perfusion time-to-peak of the lesions was  $40.8 \pm 12.3$  s. The intensity enhancement caused by the contrast agent was stable for about 20–30 s. The average scanning time of a 3-D volume was 3.5 s, thus considerably fast if compared with the duration stability of the intensity enhancement. This ensured an optimal representation of the intra-nodular intensity enhancement.

Figure 6 reports the HRUS (Fig. 6a), color Doppler (Fig. 6b) and CEUS (Fig. 6c) of a benign nodule (goiter nodule). Figure 7 reports the 3-D reconstruction of the skeleton (Fig. 7a) and the overlay of a single slice of the skeleton on the corresponding CEUS image (Fig. 7b). The benign lesion shows an enhancement lower than the surrounding healthy tissue. The skeleton of the malignant nodule (Fig. 8a and b) is clearly richer than that of the benign (Fig. 8c and d). The malignant lesion has a greater NT value (83.1 against 18.1 of the benign), a more dense vascular structure (VD for the tumor is equal to 0.04 against 0.01 of the benign lesion), a higher NB (1453 against 552) and increased values of DM (51 against 18), ICM (19.9 against 8.7) and SOAM (26 against 11). The average vessel radius MR resulted almost equal (1.8 for both).

Table 1 reports the average skeleton values measured on the sample population, showing that the

malignant nodules had higher values of NT, VD, NB and SOAM. The MR, DM and ICM parameters resulted higher in carcinomas but not at a significant level. We performed an outlier removal procedure (based on the Mahalanobis distance and the  $T^2$  Hotelling test) and we found no outliers in the malignant and one outlier in the benign group. We removed the outlier and re-ran the Mann-Whitney U-test. This experiment showed that DM and ICM parameters became statistically different between the malignant and benign populations. The new values of DM and ICM after outlier removal were  $17.9 \pm 10.9$  and  $8.6 \pm 6.5$ , respectively.

The algorithms for preprocessing, skeletonization and computation of the skeleton characteristics were implemented in MATLAB environment (TheMathWorks, Natick, MA, USA) and required on average  $100 \pm 12$  min of processing. We are in a process of porting the scientific system toward faster commercial version.

## DISCUSSION AND CONCLUSION

We presented a strategy for the processing of 3-D contrast-enhanced ultrasound images of single thyroid lesions. Morphologic operations were coupled to a thinning technique to obtain a minimal representation of the lesion vasculature. We preferred to use manual instead of mechanically driven scanning. This is mainly due to: (1) almost negligible bulkiness and (2) relatively higher cost of the motor controlled systems and maintenance.

From a technical point of view, our procedure proved robust in processing the 3-D CEUS images and in extracting the corresponding skeleton. We used a combination of distance transform and Ma and Sonka method (Ma and Sonka 1996) to optimize the thinning algorithm of our volumes. We also optimized the threshold parameter  $T_p$  to ensure the optimal representation of the nodule inner vasculature without allowing disconnected patterns. The value of  $T_p$  was critical. If the  $T_p$  value was low, a point

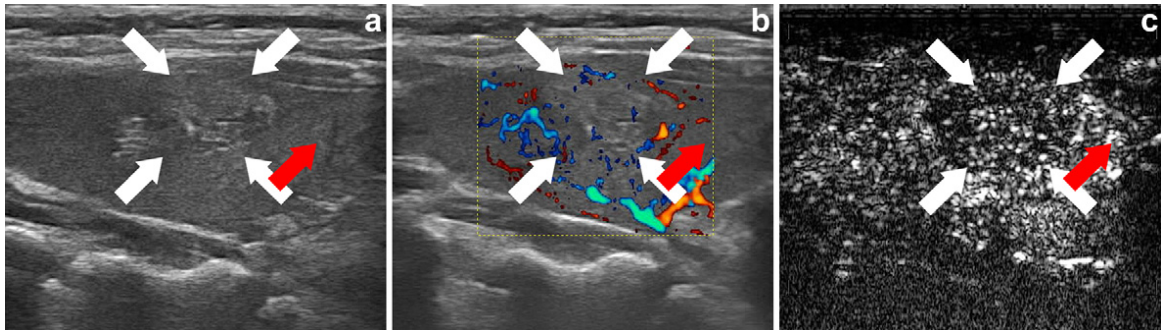


Fig. 6. (a) High-resolution ultrasonography (HRUS) of a benign lesion (goiter nodule). The white arrows indicate the position of the lesion; the red arrow indicates healthy thyroid parenchyma. (b) Color Doppler image of the goiter nodule showing a weak vascularization (white arrows) compared with healthy tissue (red arrow). (c) Contrast-enhanced ultrasound imaging (CEUS) image of the goiter nodule. The lesion shows a low enhancement (white arrows) if compared with healthy parenchyma (red arrow).



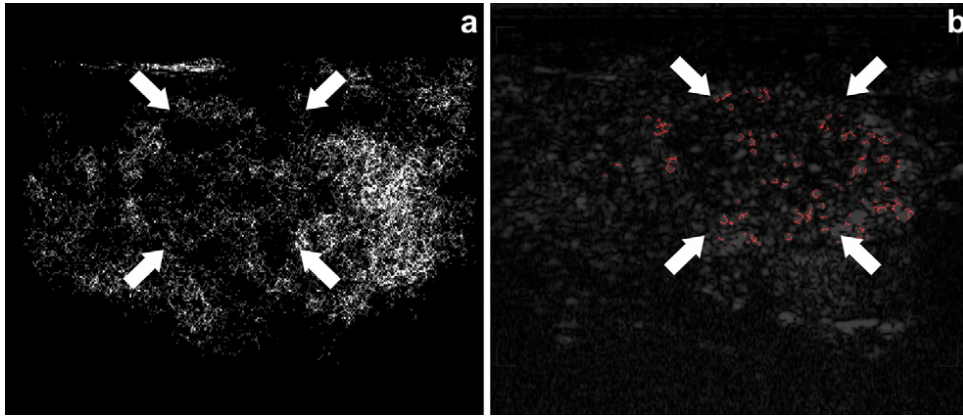


Fig. 7. (a) Maximum intensity projection of the 3-D skeleton. (b) Contrast-enhanced ultrasound imaging (CEUS) image of a goiter nodule with corresponding skeleton overlaid in red. The white arrows indicate the nodule position. The lesion shows lower vascularity than healthy thyroid tissue.

was assigned to the skeleton if its  $DT$  value is slightly higher than that of its neighborhood. Conversely, if the value of  $T_p$  was high, a point is assigned to the skeleton if and only if the  $DT$  value is substantially higher than that of its neighborhood. Hence, higher  $T_p$  values produce a very selective skeleton, resulting in a strong thinning of

the image. The probability of obtaining disconnected points increases when the  $T_p$  value increases. We kept  $T_p$  value same for all the subjects.

This procedure was semiautomatic. Two points were manually selected: darkest and brightest spots in the image, representing the presence (perfused zone) and

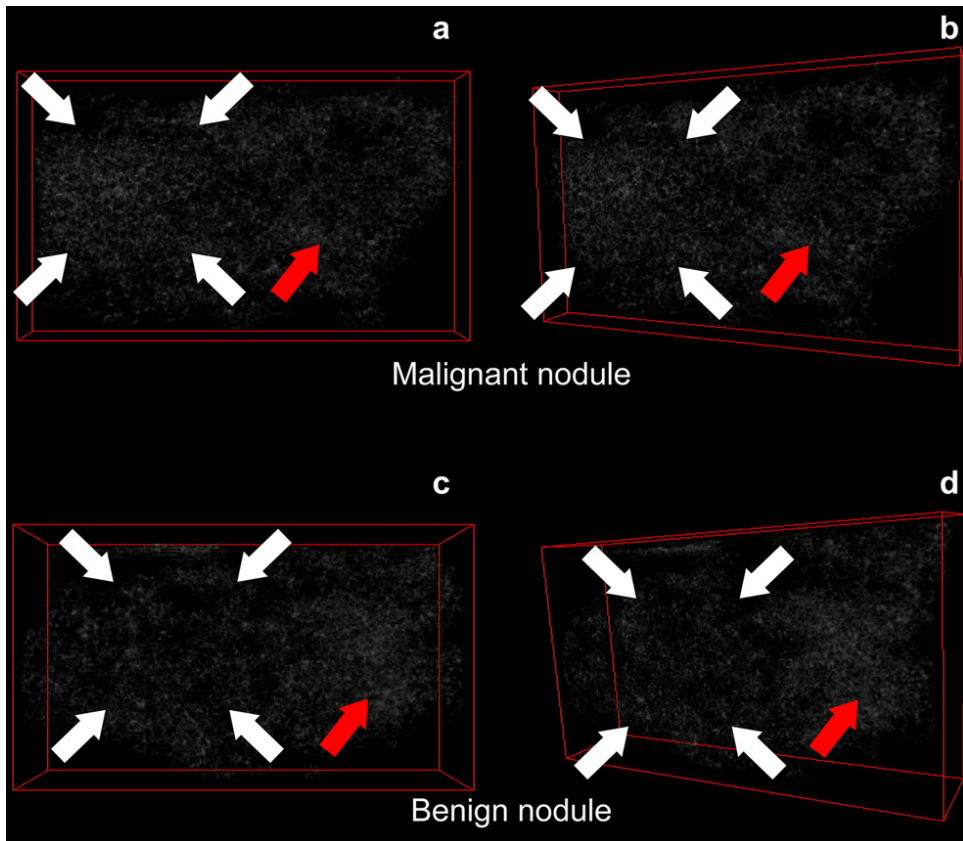


Fig. 8. (a) and (b) 3-D skeleton representation of a malignant nodule (papillary carcinoma). The white arrow indicates the nodule position, whereas the red arrow indicates a portion of healthy thyroid parenchyma of the same lobe. Note that the nodule has a brighter appearance with respect to normal tissue, thus indicating increased vascularity. (c) and (d) 3-D skeleton of a benign nodule (goiter). Note that the nodule has a lower enhancement with respect to normal tissue, thus showing a weak vascularization.

Table 1. Average values of the seven skeleton characteristics measured on the sample population of 10 patients with malignant nodules (first row) and 10 patients with benign nodules (second row)

	NT	VD	NB	MR	DM	ICM	SOAM
Malignant	76.0 ± 38.8*	0.03 ± 0.01*	1385.0 ± 796.7*	1.9 ± 1.1	47.0 ± 24.7	20.5 ± 11.7	25.9 ± 13.4*
Benign	33.2 ± 27.4	0.01 ± 0.01	659.0 ± 982.8	1.8 ± 1.1	20.8 ± 18.4	9.5 ± 6.2	10.8 ± 7.3

Skeleton parameters were: NR = number of vascular trees; VD = density of vascular structure; NB = number of branches; MR = average vessel radius; DM = 2-D tortuosity; ICM = inflection count metric; SOAM = 3-D vascular tortuosity. The asterisks in the first row indicate that the corresponding skeleton characteristic value for malignant lesions was statistically different when compared with benign (Mann-Whitney U-test,  $p < 0.05$ ).

absence (nonperfused zone) of the contrast agent. These two extreme points were used for normalization or scaling of the intensities in the rectangular ROI manually drawn by the trained operator (endocrinologist and sonographer - R.G., with 30 years of experience). A possible bias from this step could lead into erroneous ROI determination, which as a result could affect the normalization stage. An incorrect normalization could, therefore, affect the region-based segmentation. This rectangular ROI stage of the procedure is still user-dependent since the relatively low signal-to-noise ratio of the images posed some difficulties in automating this step.

The nodule in the ultrasound image was manually delineated too. Manual tracing of the boundaries was made by the same expert sonographer who performed the acquisitions. In addition, the images of the patients undergoing thyroidectomy were further evaluated by surgeons. This was a double check and helped in minimizing the tracing the errors. ROIs were manually traced too, but it was simple to place them in the middle of the lesion once the expert had outlined the nodule. The authors are now working toward the development of a completely automated processing procedure.

The skeleton parameters measured of the malignant lesions were clearly different from those of benign ones. After the outlier rejection removal, the only parameter that did not prove statistically different was MR (*i.e.*, the average radius of the vessels). Therefore, the average radius of the vessels did not differ between the benign and the malignant lesions. This result is in accordance to studies based on the color Doppler technique, which did not show evidence on differences in the vessels size in malignancy (Bozborja et al. 2002).

Conversely, malignant lesions showed a higher number of the vascular trees (NT) and the number of branches (NB). In addition, the density of the vascular structure (VD) was higher than in benign lesions. These findings suggest that malignant lesions are highly perfused by a dense vascular bed. Such vessels also originate several branches, thus, increasing the overall density of the vasculature in the lesion. This result confirms previous findings. Fukunari et al. showed that follicular carcinomas can be diagnosed by using color Doppler given their high degree of internal vascularization

(Fukunari et al. 2004). Bakhshaei et al. found that dense internal vasculature is highly correlated to malignancy (Bakhshaei et al. 2008). Turner et al., in their review, pointed out that many studies confirmed the increased vascularization of thyroid tumors with respect to normal tissue and benign lesions (Turner et al. 2003).

The use of CEUS in the diagnosis of thyroid nodules is a promising technique, even though results are still discordant. Spiezia et al. conducted a perfusion study based on color Doppler imaging after contrast agent injection (Spiezia et al. 2001). They showed that carcinomas had a lower time-to-peak of the perfusion curve but that the peak intensity and the washout were not statistically different from benign nodules. Conversely, in another study, the time-intensity CEUS curves did not prove useful in differentiating between benign and malignant nodules (Friedrich-Rust et al. 2009). Argalia et al. demonstrated that the CEUS time-intensity curves can provide an indirect description of the intra-nodular vascularization (Argalia et al. 2002). They observed that 89% of malignant nodules (characterized by an “anarchical” vascularization) had polyphasic wash-out curves, whereas benign lesions showed a monophasic curve. These studies demonstrate the diagnostic possibilities of CEUS but also manifest the need for numerical evaluation of the vascular pattern of the lesions.

Overall, our results are in agreement with the above-referenced studies. We obtained a clear indication of “anarchical” vascularization of malignant nodules, which we demonstrated and quantified by higher values of the skeleton parameters.

Whilst the dimension of our sample was relatively low, this study gave encouraging results. We are currently working to enlarge our sample population (1) enhance the statistical significance of our results; and (2) derive a classification scheme based on the skeleton parameters.

*Acknowledgments*—The study was supported by a grant from the Fondazione Scientifica Mauriziana ONLUS of Torino.

## REFERENCES

- Appetecchia M, Bacaro D, Brigida R, Milardi D, Bianchi A, Solivetti F. Second generation ultrasonographic contrast agents in the diagnosis of neoplastic thyroid nodules. *J Exp Clin Cancer Res* 2006;25: 325–330.

- Argalia G, De Bernardis S, Mariani D, Abbattista T, Taccaliti A, Ricciardelli L, Faragona S, Gusella PM, Giuseppetti GM. Ultrasonographic contrast agent: evaluation of time-intensity curves in the characterisation of solitary thyroid nodules. *Radiol Med* 2002;103:407–413.
- Bakhshaei M, Davoudi Y, Mehrabi M, Layegh P, Mirsadaee S, Rad MP, Leyegh P. Vascular pattern and spectral parameters of power Doppler ultrasound as predictors of malignancy risk in thyroid nodules. *Laryngoscope* 2008;118:2182–2186.
- Bartolotta TV, Midiri M, Galia M, Runza G, Attard M, Savoia G, Lagalla R, Cardinale AE. Qualitative and quantitative evaluation of solitary thyroid nodules with contrast-enhanced ultrasound: Initial results. *Eur Radiol* 2006;16:2234–2241.
- Bastin S, Bolland MJ, Croxson MS. Role of ultrasound in the assessment of nodular thyroid disease. *J Med Imaging Radiat Oncol* 2009;53:177–187.
- Bozboru A, Erbil Y, Ozarmagan S, Barbaros U, Sari S, Degirmenci B. Color Doppler sonography in cold thyroid nodules for malignancy prediction. *Acta Chir Belg* 2002;102:259–262.
- Carraro R, Molinari F, Deandrea M, Garberoglio R, Suri JS. Characterization of thyroid nodules by 3-D contrast-enhanced ultrasound imaging. *Conf Proc IEEE Eng Med Biol Soc* 2008;2008:2229–2232.
- Chen Z, Molloy S. Vascular tree object segmentation by deskeletonization of valley courses. *Comput Med Imaging Graph* 2002;26:419–428.
- D'Souza MM, Marwaha RK, Sharma R, Jaimini A, Thomas S, Singh D, Jain M, Bhalla PJ, Tripathi M, Tiwari A, Mishra A, Mondal A, Tripathi RP. Prospective evaluation of solitary thyroid nodule on 18F-FDG PET/CT and high-resolution ultrasonography. *Ann Nucl Med* 2010;24:345–355.
- Friedrich-Rust M, Sperber A, Holzer K, Diener J, Grunwald F, Badenhop K, Weber S, Kriener S, Herrmann E, Bechstein WO, Zeuzem S, Bojunga J. Real-time elastography and contrast-enhanced ultrasound for the assessment of thyroid nodules. *Exp Clin Endocrinol Diabetes* 2009 Oct 23 [Epub ahead of print].
- Fukunari N, Nagahama M, Sugino K, Mimura T, Ito K. Clinical evaluation of color Doppler imaging for the differential diagnosis of thyroid follicular lesions. *World J Surg* 2004;28:1261–1265.
- Gorce JM, Arditi M, Schneider M. Influence of bubble size distribution on the echogenicity of ultrasound contrast agents: A study of SonoVue. *Invest Radiol* 2000;35:661–671.
- Hoang JK, Lee WK, Lee M, Johnson D, Farrell S. US features of thyroid malignancy: pearls and pitfalls. *Radiographics* 2007;27:847–860. discussion 61–65.
- Huang SF, Chang RF, Moon WK, Lee YH, Chen DR, Suri JS. Analysis of tumor vascularity using three-dimensional power Doppler ultrasound images. *IEEE Trans Med Imaging* 2008;27:320–330.
- Ivanac G, Brkljacic B, Ivanac K, Huzjan R, Skreb F, Cikara I. Vascularisation of benign and malignant thyroid nodules: CD US evaluation. *Ultraschall Med* 2007;28:502–506.
- Loizou CP, Pattichis CS, Christodoulou CI, Istepanian RS, Pantziaris M, Nicolaides A. Comparative evaluation of despeckle filtering in ultrasound imaging of the carotid artery. *IEEE Trans Ultrason Ferroelectr Freq Control* 2005;52:1653–1669.
- Ma MC, Sonka M. A fully parallel 3-D thinning algorithm and its applications. *Comput Vis Image Understanding* 1996;64:420–433.
- Mihai R, Parker AJ, Roskell D, Sadler GP. One in four patients with follicular thyroid cytology (THY3) has a thyroid carcinoma. *Thyroid* 2009;19:33–37.
- Molinari F, Carraro R, Deandrea M, Garberoglio R. Skeletonization of 3-D contrast enhanced ultrasound images for the accurate characterization of thyroid nodules. In: Group NB, (ed). *First Italian National Congress of Bioengineering*. Pisa, July 3-5, Pàtron Editore; 2008. p. 593–594.
- Palàgyi K, Kuba A. A 3-D 6-subiteration thinning algorithm for extracting medial lines. *Pattern Recognition Lett* 1998;19:613–627.
- Polyzos SA, Kita M, Avramidis A. Thyroid nodules - Stepwise diagnosis and management. *Hormones (Athens)* 2007;6:101–119.
- Spiezia S, Farina R, Cerbone G, Assanti AP, Iovino V, Siciliani M, Lombardi G, Colao A. Analysis of color Doppler signal intensity variation after levovist injection: A new approach to the diagnosis of thyroid nodules. *J Ultrasound Med* 2001;20:223–231. quiz 33.
- Turner HE, Harris AL, Melmed S, Wass JA. Angiogenesis in endocrine tumors. *Endocr Rev* 2003;24:600–632.
- Wang T, Basu A. A note on 'A fully parallel 3-D thinning algorithm and its applications'. *Pattern Recognition Letters* 2007;28:501–506.
- Zhang B, Jiang YX, Liu JB, Yang M, Dai Q, Zhu QL, Gao P. Utility of contrast-enhanced ultrasound for evaluation of thyroid nodules. *Thyroid* 2010;20:51–57.